A Data-Model Comparative Study of Ionospheric Positive Storm Phase in the Midlatitude *F* Region

G. Lu,[1] L. P. Goncharenko,[2] A. J. Coster,[2] A. D. Richmond,[1] R. G. Roble,[1]
N. Aponte,[3] and L. J. Paxton[4]

A strong positive storm phase was observed by both the Millstone Hill and Arecibo incoherent scatter radars during a moderate geomagnetic storm on 10 September 2005. The positive storm phase featured an interesting UT–altitude profile of the *F* region electron density enhancement that closely resembles the Greek letter Λ. The radar measurements showed that the uplift of the electron density peak height corresponded to a strong upward ion drift, whereas the subsequent falling of the peak height coincided with a downward ion drift. Using realistic, time-dependent ionospheric convection and auroral precipitation as input, the thermosphere–ionosphere electrodynamics general circulation model (TIEGCM) is able to reproduce the same Λ-like structure in the electron density profile, along with many large-scale features in electron temperature and vertical ion drift as observed by the radars. Over the 3-day period of 8–10 September, our simulation results show an error of 1%–4% for h_mF_2, electron, and ion temperatures at both radar locations. The estimated error for N_mF_2 is about 9% at Millstone Hill and 19% at Arecibo. However, the simulated vertical ion drifts are less accurate, with the normalized root-mean-square errors of 72% at Millstone Hill and 52% at Arecibo, due largely to model's inability to capture the large temporal fluctuations measured by the radars. However, it reproduces reasonably well the overall large-scale variations during the 3-day period, including the storm-time-enhanced upward ion drift that is responsible for the interesting *F* region density profile. The model is also able to reproduce the temporal and spatial total electron content variations as shown in the global GPS maps. The comparison with the GUVI O/N_2 is less satisfactory, although there is a general agreement in terms of relative O/N_2 changes during the storm in the longitudinal sector between 60°W and 80°W where the radars are located. The detailed data–model comparison carried out in this study is helpful not only to validate the model but also to interpret the complex observations. The

Midlatitude Ionospheric Dynamics and Disturbances
Geophysical Monograph Series 181

10.1029/181GM07

[1]High Altitude Observatory, National Center for Atmospheric Research, Boulder, Colorado, USA.
[2]Haystack Observatory, Massachusetts Institute of Technology, Westford, Massachusetts, USA.
[3]Arecibo Observatory, Arecibo, Puerto Rico, USA.
[4]Applied Physics Laboratory, Johns Hopkins University, Laurel, Maryland, USA.

TIEGCM simulations reveal that it is the enhanced meridional neutral wind, not the penetration electric field, that is the primary cause of the Λ structure of the *F* region electron density profile.

1. INTRODUCTION

Ionospheric disturbances are often categorized as a positive or negative storm phase if there is an increase or decrease of the *F* region peak electron densities with respect to their quiet time values. It is well-known that ionospheric storm effects are determined by a combination of chemical, dynamic, and electrodynamic processes. Increased O_2 and N_2 densities result in increased conversion of O^+ to O_2^+ and NO^+, which then rapidly recombine with electrons, resulting in a rapid decrease in electron density [*Rishbeth*, 1989; *Burns et al*., 1995]. Although neutral composition changes are often attributed to the formation of a negative storm phase [*Prölss*, 1993], several studies have shown a positive storm phase as a result of a large increase in the O/N_2 ratio [e.g., *Burns et al*., 1995; *Field et al*., 1998]. Magnetospheric electric fields associated with a strongly southward interplanetary magnetic field (IMF) are most effective in producing large geomagnetic storms. They drive strong ion convection in the high-latitude polar regions, and a fraction of magnetospheric electric fields can penetrate to middle and low latitudes, prompting nearly simultaneous ionospheric disturbances there. The fast-moving ions driven by magnetospheric electric fields at high latitudes collide with neutrals to produce frictional heating or joule heating. The excessive joule heating dissipation in the high-latitude polar regions produces large pressure gradients that drive neutral winds equatorward toward middle and low latitudes, even into the opposite hemisphere. An enhanced equatorward (poleward) meridional wind pushes plasma up (down) along magnetic field lines due to their inclination with respect to Earth's surface, raising or lowering the *F* region electron density peak height accordingly. In addition, a polarization electric field can be created in the midlatitude regions by the storm-enhanced neutral winds to form the "disturbance dynamo" effect [*Blanc and Richmond*, 1980]. In a real storm event, several different processes may work in concert. Also, because of the complex interaction among the different processes, it is often very difficult to distinguish the effects of one process from another.

While the effects of neutral wind dynamics on ionospheric storms are fully recognized (see reviews by *Prölss* [1995], *Buonsanto* [1999], and *Mendillo* [2006]), in recent years, more attention has been paid to the prompt penetration electric fields, partly due to the fact that major geomagnetic storms tend to be associated with a strong southward IMF. *Huang et al*. [2005b] showed several cases in which the penetration electric field can last several hours after the IMF turns southward and geomagnetic activity remains high. The large penetration electric fields produce the so-called superfountain effect, which significantly intensifies the total electron content (TEC) [e.g., *Tsurutani et al*., 2004; *Mannucci et al*., 2005] and are found to be a primary cause of the dayside positive storm phase [e.g., *Huang et al*., 2005a]. Therefore, the storm effects produced by such long-lasting penetration electric fields may have overshadowed the relatively weaker effects of disturbance neutral winds during major storms.

In this paper, we expand the work by *Lu et al*. [in press] on a moderate geomagnetic storm taking place on 10 September 2005. The event was depicted by a very interesting feature in the *F* region electron density profile that closely resembles the Greek letter Λ. The observational aspect of the event has been discussed in detail by *Goncharenko et al*. [2007]. Here we focus our attention on comparison of the simulation results from the Thermosphere–Ionosphere Electrodynamics General Circulation Model (TIEGCM) [*Richmond et al*., 1992] with measurements obtained from two incoherent scatter radars located in the lower and higher midlatitudes, with Arecibo in Puerto Rico and Millstone Hill in Massachusetts, as well as with those from the global GPS receivers and the TIMED/GUVI instrument. Through such a comprehensive data–model comparison, we will not only validate our model's performance but also shed some new light on the underlying physical processes that are responsible for the Λ-shaped *F* region electron density variation.

It should be pointed out that a very similar Λ structure in the electron density profile was reported by *Roble et al*. [1978] during the September 1974 geomagnetic storm. Using a simplified two-dimensional (e.g., latitude versus altitude) thermospheric and ionospheric model, they concluded that the positive storm phase was produced by gravity waves generated by impulsive heating over the polar cap region. However, in that study, the heat source (assumed to be primarily joule heating) distribution as well as its temporal variation were prescribed to match the observed ionospheric property. In this study, we will use the more advanced three-dimensional model of the TIEGCM, along with more realistic magnetospheric energy inputs derived from the as-

similative mapping of ionospheric electrodynamics (AMIE) procedure [*Richmond and Kamide*, 1988], to reexamine the conclusions made by *Roble et al*. [1978].

2. OBSERVATIONS AND MODEL COMPARISON

2.1. Geophysical Conditions and Model Inputs

The solar wind and geophysical conditions for the 8–10 September 2005 period are shown in Figure 1. The solar wind parameters measured by the ACE satellite have been time-shifted by 36 min to account for the solar wind propagation time required from the upstream location to the dayside magnetopause. From 0400 UT on 8 September until ~1400 UT on 9 September, the magnitude of IMF B_z was less than 5 nT. As a result, the geophysical condition of the ionosphere and magnetosphere was quiet, as indicated by the small values of *Dst*, *AE*, the polar cap potential drop and the power inputs of joule heating and auroral precipitation. Around 1400 UT on 9 September, an interplanetary shock arrived, along with a rapid increase in solar wind dynamic pressure. The pressure impulse prompted a storm sudden commencement as shown by the positive excursion in *Dst*, together with increases in *AE*, the polar cap potential drop and joule heating dissipation. The geophysical disturbances associated with the solar wind dynamic pressure impulse are interesting but not the focus of this study. Here we concentrate on the disturbance during the second half day on 10 September when a moderate geomagnetic storm took place following a southward turning of the IMF near 1600 UT. The storm had a minimum *Dst* value of about −70 nT and a maximum *AE* value of ~2500 nT. The cross polar cap potential drop and the hemispheric integrated joule heating both increased after the IMF turned southward. The magnitude of the hemispheric integrated joule heating rate was much larger in the northern hemisphere than in the southern hemisphere. As discussed by *Lu et al*. [in press], this hemispheric difference is due in part to the relatively sparse data coverage in the southern hemisphere, which resulted in smaller electric potential drops because of the interpolation of the limited data points when applying the AMIE procedure [*Lu et al*., 1996]. The increase in auroral electron energy flux was rather subtle, and the hemispheric integrated auroral power was substantially smaller than joule heating dissipation during the event.

To simulate the ionospheric and thermospheric response to this moderate geomagnetic storm, we have used the realistic, time-dependent high-latitude ionospheric convection and auroral precipitation patterns derived from AMIE. The data input to AMIE was obtained from various space- and ground-based observations, including those from the

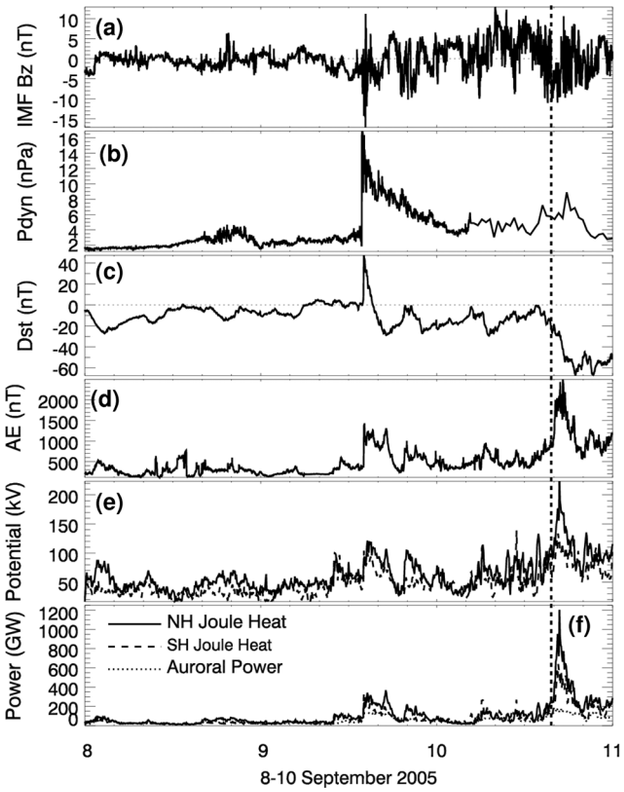

Figure 1. Distributions of the (a) IMF B_z component, (b) solar wind dynamic pressure, (c) *Dst* index, (d) *AE* index, (e) cross polar cap electric potential drop in the northern (solid line) and southern (dashed line) hemisphere, and (f) hemispheric integrated joule heating over the northern hemisphere (solid line) and southern (dashed line) and the northern hemispheric integrated auroral power (dotted line). The vertical dashed line marks the onset of the geomagnetic storm at about 1600 UT on 10 September.

Defense Meteorological Satellite Program (F13, 15, and 16) and NOAA (NOAA 15, 16, and 17) satellites, 12 Super Dual Auroral Radar Network radars (10 in the northern hemisphere and 2 in the southern hemisphere), and 178 ground magnetometers. Patterns of ionospheric convection, auroral electron energy flux, and characteristic energy, along with many other ionospheric electrodynamic fields, were derived in a 5-min cadence over both northern and southern hemispheres. The AMIE patterns were timely interpolated to drive the TIEGCM, which ran in a 2-min time step. Solar EUV and UV fluxes (which have a 1-min time resolution) were obtained from the empirical flare irradiance spectral model (FISM) [*Chamberlin et al*., 2007] to replace the traditional F10.7 proxy (which is a daily average) for this particular event. At the lower boundary, the model incorporates the

amplitudes of diurnal and semidiurnal tides at the model's lower boundary based on the global scale wave model [*Hagan and Forbes*, 2002]. For this study, we used the coarse-grid version of the TIEGCM, which has an effective 5° × 5° latitude–longitude grid with 29 constant pressure levels, extending from about 97 km up to 500–800 km, depending on solar cycle conditions. This study mainly concerns the altitude range between 100 and 500 km where the radar measurements were obtained.

2.2. Comparison With Radar Measurements

Plate 1 shows the measured and simulated electron density *Ne*, electron temperature *Te*, and vertical ion drift *Wi* over Millstone Hill from 1000 to 2400 UT on the quiet day of 8 September (left) and on the storm day of 10 September (right), respectively. The Millstone Hill radar is located at 42.6°N and 71.5°W, and the local time (LT) corresponds roughly to UT − 5. In comparison with the quiet day *Ne* distribution, there was a significant increase of *Ne* in the *F* region between ~1600 and 2300 UT on the storm day of 10 September, along with the increase of the *F* region peak height h_mF_2. The most striking feature is the UT–altitude profile of the *Ne* enhancement, which closely resembles the Greek letter Λ. Accompanied by the increase in *Ne* was a decrease in *Te.* The anticorrelation between *Te* and *Ne* is fully anticipated since the electron cooling rate is proportional to *Ne* [*Schunk and Nagy*, 2000]. The ion temperature (not shown), on the other hand, increased slightly during the storm [*Goncharenko et al*., 2007]. The measured vertical ion drift showed a large upward motion starting at ~1640 UT, which coincided with the initial uplift of h_mF_2. The ion drift then became downward at 1900 UT, about the same time when h_mF_2 started to fall.

At first glance, the TIEGCM simulations appear to be in a good quantitative agreement with the Millstone Hill radar measurements on both quiet and storm days. A similar Λ-like structure in the UT–altitude distribution of *Ne* is very well reproduced by the model, as is the anticorrelation between the simulated *Ne* and *Te*. There are, however, some qualitative differences between the observed and simulated *Ne*. For example, the simulated *F* region *Te* on 8 September starts to decrease too fast compared with the radar-measured *Te* shown in Plate 1c. However, during the storm, the simulations show a generally good agreement with the measurements, except for a short period around 2200 UT when the simulated *Te* becomes cooler by a few hundreds of degrees than the measured *Te*.

The simulated vertical ion drift also shows many large-scale features consistent with the radar observations. On the quiet day as well as prior to the storm onset, the Millstone Hill radar observed upward ion drift above ~350 km. Similar upward ion drift is seen in the simulations but at higher altitudes, mostly above 450 km. The prestorm upward ion drift, as found in the simulations, is associated with ion diffusion derived by the imbalance between the upward plasma pressure gradient force and the downward gravitational force on the plasma. At 1640 UT on 10 September, the time when the Millstone Hill radar started to observe strong upward ion drift, the simulation also shows a temporarily enhanced upward drift above 300 km followed by a more pronounced upward ion drift about 10 min later. In the region below 250 km, however, the simulated strong upward ion drift (> 25 m/s) lags behind the radar measurements by nearly 40 min.

Plate 2 shows the similar data–model comparison but over Arecibo. The Arecibo radar is at 18.3°N and 66.7°W and LT = UT − 4.4. It observed a similar Λ-like structure in the *Ne* profile as the Millstone Hill radar did. The rise of h_mF_2 at Arecibo was delayed until ~1750 UT, again coincident with the enhanced upward ion drift. The time delay in the initial uplift of h_mF_2 between Millstone Hill and Arecibo implies a propagation speed of 680 m/s for the traveling ionospheric disturbance (TID). The anticorrelation between *Ne* and *Te* was more pronounced in the Arecibo measurements.

The simulated *Ne* is in reasonably good agreement with the radar measurements. However, the simulations do not show the measured temporal density drop around 2100 UT on 8 September, and the simulated *Ne* is too large compared with the measured *Ne* in the upward lag of the Λ structure. The simulated *Te* is also in a good agreement with the measured *Te* on both the quiet day and the storm day. The simulated vertical ion drift agrees well with the measurements on 8 September. On 10 September, the prestorm *F* region vertical ion drift consisted of a strong downward flow, followed by a strong upward flow. The simulations display a similar downward-to-upward change in vertical ion drift at ~1030 UT, about 1 h too early with respect to the radar observations. A better agreement between the measured and simulated drifts is found after 1800 UT over Arecibo, including the hockey-stick-like structure of strong upward ion drift followed by downward ion drift.

To assess the model performance in a more quantitative fashion, we follow the same approach proposed by *Pawlowski et al*. [2008] who carried out a detailed data–model comparison for the entire month of September 2005, including the storm interval that we are analyzing here. Figure 2 shows the comparison of the observed and simulated parameters at the *F* region peak height, since h_mF_2 is commonly considered as a good representative of the *F* region variations during storms. The normalized root-mean-square (RMS) error and the cross-correlation coefficient (corr) of the model outputs are shown in each panel. According to

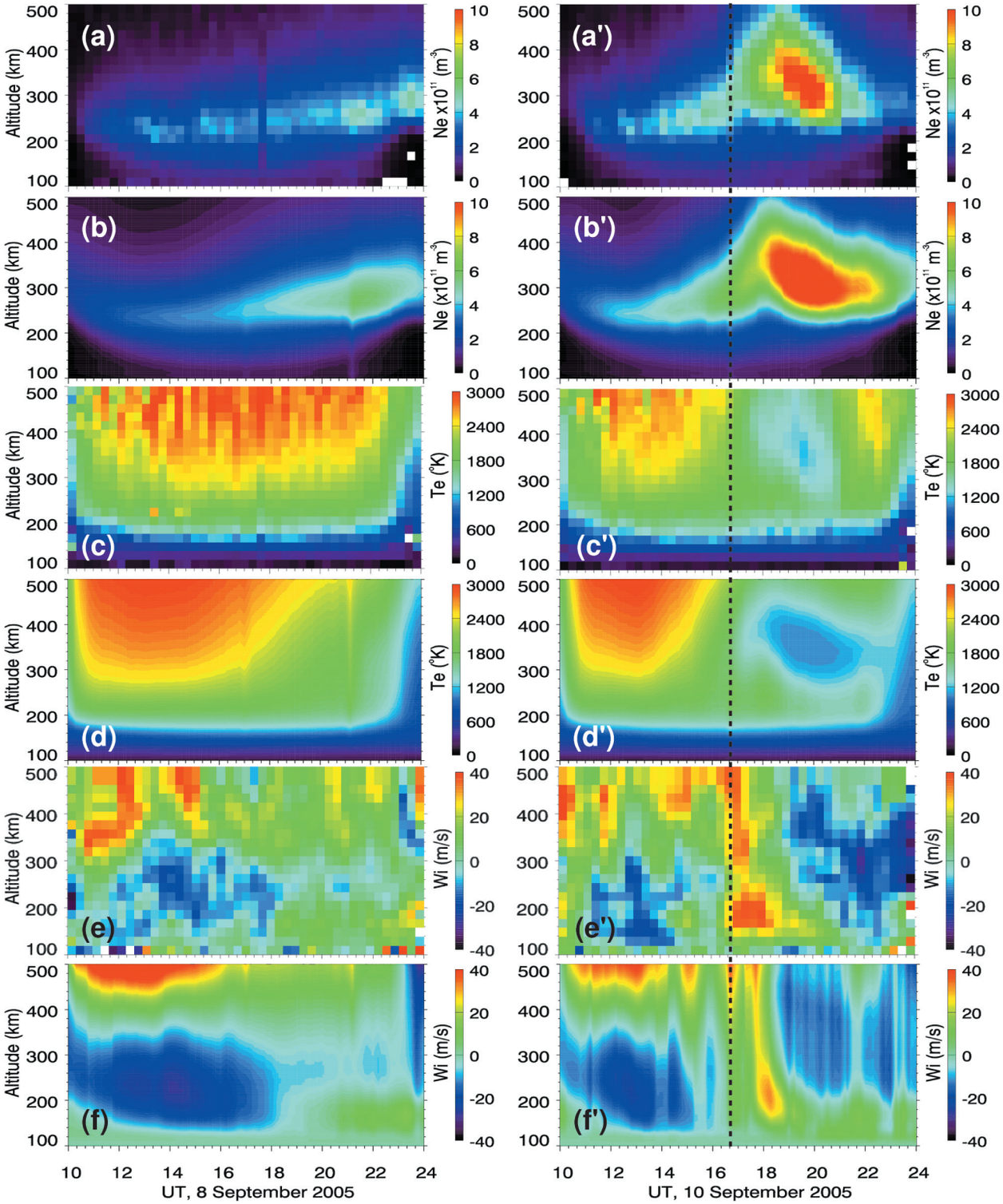

Plate 1. UT–altitude profiles of (a) measured electron density, (b) simulated electron density, (c) measured electron temperature, (d) simulated electron temperature, (e) measured vertical ion drift, and (f) simulated vertical ion drift for the (left) quiet day on 8 September and (right) storm day on 10 September over Millstone Hill. The vertical dashed line denotes the onset of upward lift of the electron density peak height.

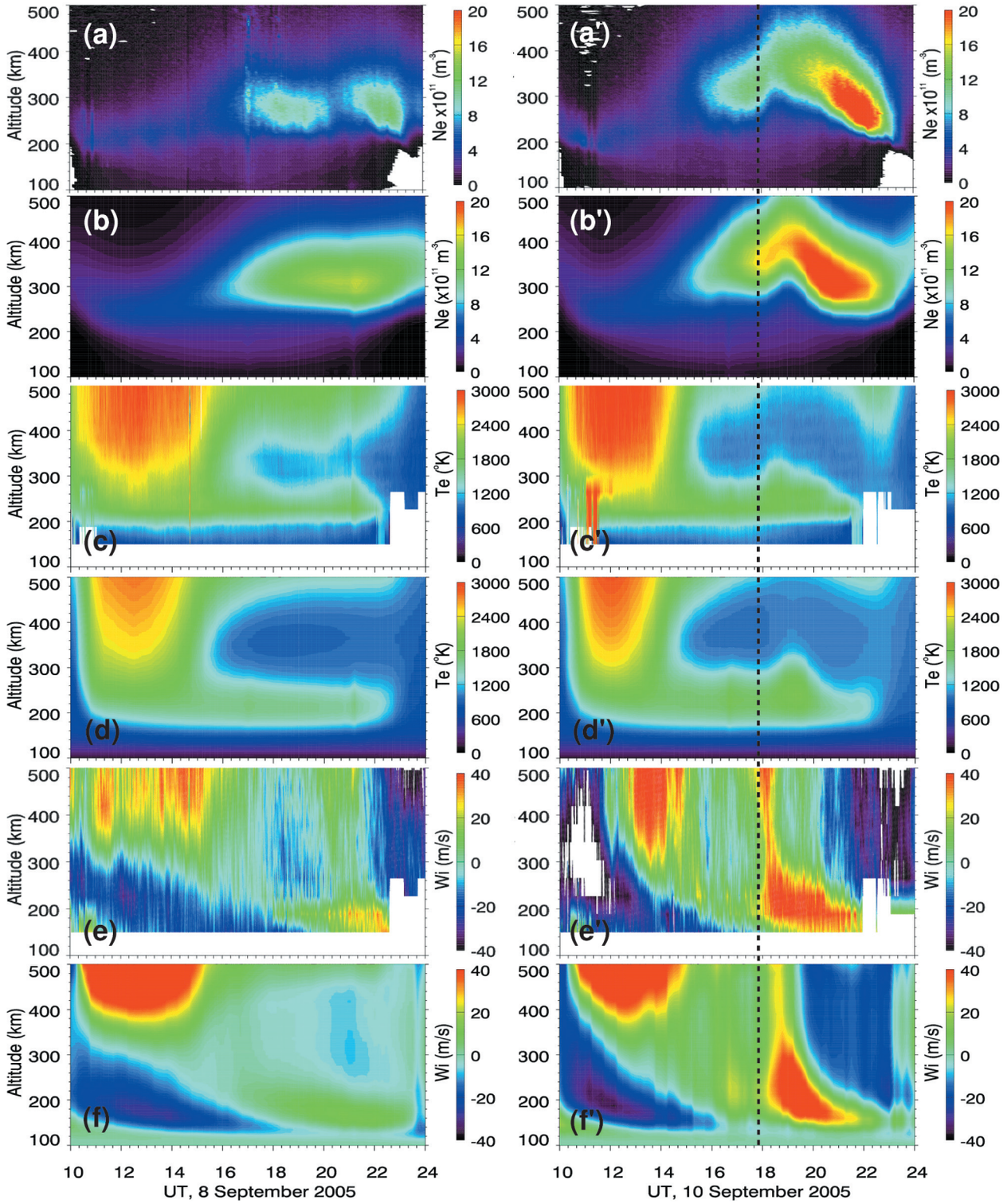

Plate 2. Similar to Plate 1, but over Arecibo.

Pawlowski et al. [2008], the normalized RMS error is defined as $\sqrt{\langle (F_{\text{model}} - F_{\text{data}})^2 \rangle} / \sqrt{\langle F_{\text{data}}^2 \rangle}$, where $\langle\ \rangle$ symbolizes taking a mean and F denotes a given parameter (e. g., the electron density, temperature, vertical ion drift). At Millstone Hill, the normalized RMS errors are about 1%–3%, except for the vertical ion drift, for which the error is substantially large at 72%. Our normalized RMS errors for the density and temperature are about an order of magnitude smaller than what *Pawlowski et al.* [2008] showed for their model validation. At Arecibo, our normalized RMS errors are 2% for h_mF_2, 19% for N_mF_2, 4% for *Te*, and 1% for *Ti*, but 52% for *Wi*. The large error in the simulated *Wi* at Millstone Hill is mainly associated with the large fluctuations in the observed *Wi* that the model is unable to capture partly due to the coarse grid size of our global model. On the other hand, the retrieval of the *F* region vertical ion drifts by IS radars may also be subject to some uncertainties [e.g., *Aponte et al.*, 2005]. Despite that, the model seems to do a reasonably good job in reproducing the general behavior of the vertical ion drift for the 3-day period, including the large upward drift during the storm on late September 10. The cross-correlation coefficients are around 0.70–0.90 for the density and temperature, which again are better than the values shown by *Pawlowski et al.* [2008]. However, the cross-correlation coefficient is somewhat lower (0.41 and 0.66 at the two radar locations, respectively) for *Wi*.

2.3. Comparison With GPS TEC Measurements

Plate 3 shows the comparison between the GPS TEC measurements and the simulated TEC from the TIEGCM. These TEC maps are plotted in a fixed local time range between 0400 and 2000 LT, as there was not much activity on the nightside. Although the GPS TEC maps suffer from the lack of data over the vast Pacific and Atlantic oceans, some storm-related TEC changes were discernible, particularly over the Central and North American sector (highlighted by the square box) and in the South Pacific region (highlighted by the oval-shaped area). There was a gradual increase in TEC in both these regions, with a maximum TEC enhancement reached around 2100 UT on 10 September.

There are some similarities between the simulated and observed TEC features, such as the TEC enhancements in the American and South Pacific regions. In the GPS maps, the

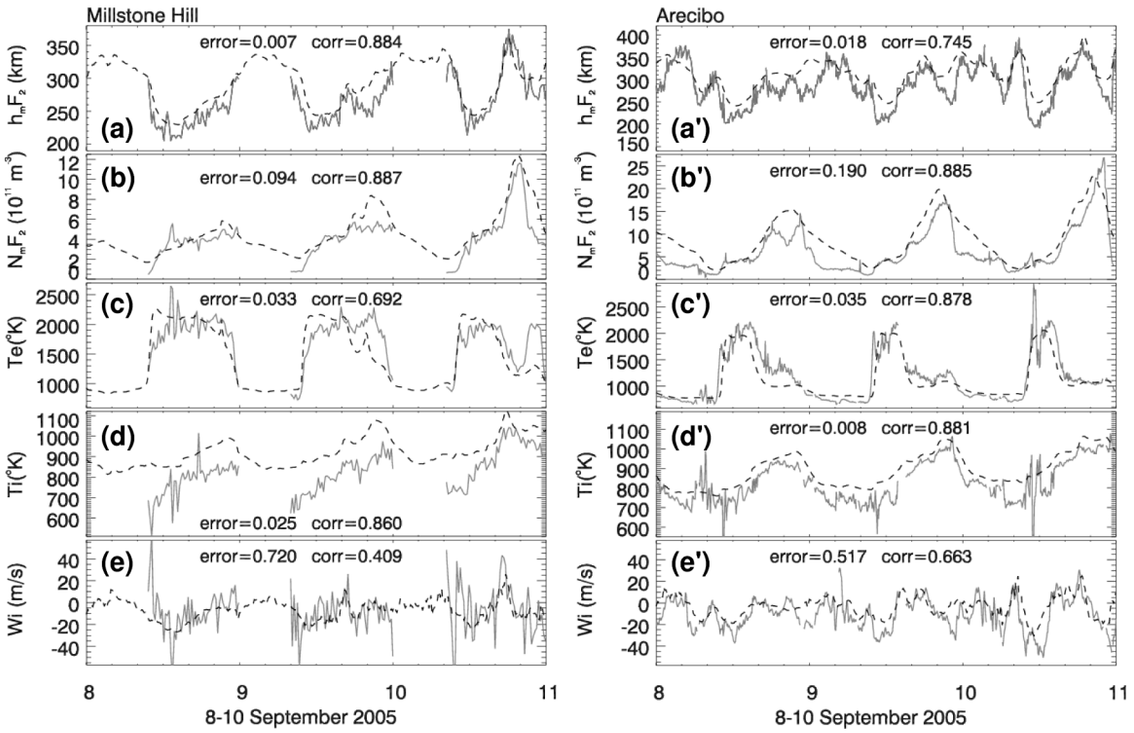

Figure 2. Comparison of observed (solid lines) and simulated (dashed lines) (a) and (a′) h_mF_2, (b) and (b′) N_mF_2, (c) and (c′) electron temperature *Te* at h_mF_2, (d) and (d′) ion temperature *Ti* at h_mF_2, and (e) and (e′) vertical ion drift *Wi* at h_mF_2 over (left) Millstone Hill and (right) Arecibo. The values of the normalized RMS error (error) and the cross-correlation coefficient (corr) are listed in each panel.

TEC enhancement over South Pacific appeared as a locally confined structure; in the model, it appears as a westward, slow-moving structure originated near the western edge of South America. From 1700 UT to 2100 UT, near Central America, the observed TEC increased from ~30 to over 70 TECU. In the simulation, TEC increases from ~25 to ~50 TECU. An important difference between the GPS TEC maps and the simulated TEC maps is that the simulated TEC values in the middle- and low-latitude regions are about 15%–35% smaller than the observations. This underestimation is partly due to the altitude limit of the TIEGCM (its upper boundary altitude is about 570 km for this storm, which took place near solar-minimum conditions).

2.4. Comparison With GUVI O/N_2 Measurements

Plate 4 shows the percent difference distributions of the ratio between the height integrated O and N_2 density, with the GUVI measurements shown on the top, and the simulation results that have been spatially and temporally extracted along the satellite track shown on the bottom. The comparison represents the percent change of O/N_2 on 10 September with respect to the quiet day of 8 September. There is some degree of agreement between the measurement and simulation in terms of the general morphology, for example, a depletion of O/N_2 over most parts of the northern and southern polar regions and a minor increase (~10%) for most of the middle-to-low-latitude region. An increase of O/N_2 is seen by both observations and simulations at the northern edge of Canada as well as between the longitude range of 120°W and 160°W, although the model results appear as much larger-scale structures. In the GUVI plot, there was a ~20% increase just off the U.S. east coast and ~20° eastward. A similar O/N_2 increase can be found in the simulations as well, but about 10° further eastward. In general, the agreement is reasonable in the longitude sector between 60°W and 80°W where the Millstone Hill and Arecibo radars are located. There are, of course, many qualitative differences between the measurements and simulations, particularly a pair of positive and negative O/N_2 changes over North America, in the simulation that cannot be found in the GUVI data.

3. DISCUSSION

The detailed data and model comparison shown in the previous section assure us that the coupled AMIE–TIEGCM has captured reasonably well some large-scale storm features in the *F* region. In this section, we attempt to explore the underlying physical mechanisms responsible for the observed ionospheric storm effects with the help of the numerical simulations.

As pointed out in the Introduction, neutral composition changes are known to play an important role in producing ionospheric disturbances during geomagnetic storms. To verify whether the composition change is a controlling factor in this case, *Lu et al.* [in press] compared the percent changes in *Ne* with the percent changes in O/N_2 [see *Lu et al.*, in press, Figure 4] and found no direct correlation between the electron density increase and the O/N_2 enhancement, implying that the composition changes are not the main cause of this particular positive storm phase. This conclusion is also consistent with the finding of *Goncharenko et al.* [2007] that the O/N_2 change played only a minor role in producing the observed positive storm phase. The weak compositional effect shown in this case is not surprising. As described by *Prölss* [1993], the equatorward transport of composition bulge is more pronounced in the postmidnight sector, where the storm-generated neutral winds are predominantly equatorward due to less interference by the poleward background winds present during daytime.

We now turn our attention to the possible effect that dynamic and electrodynamic processes may have on the observed ionospheric disturbances. The simulated vertical ion drift shown in Plates 1f and 2f is the sum of all contributions from the electric fields, meridional neutral wind, and ion diffusion [i.e., *Schunk and Nagy*, 2000]. To assess the relative contribution of neutral wind and the electric fields to vertical ion drift, Plates 5a to 5c shows the meridional wind, the vertical ion drift component due to meridional wind, and the vertical ion drift due to the electric field, respectively. As expected, the wind-driven vertical ion drift and the meridional wind are anticorrelated in the midlatitude region. Compared with the total vertical ion drift shown in Plates 1f and 2f, it is evident that storm-time vertical ion drift is primarily driven by the meridional wind surges. There are no significant changes in the electric field driven ion drift except for a very brief period around 1640 UT in both Millstone Hill and Arecibo. This temporal increase in upward ion drift is a result of the magnetospheric electric field penetration to midlatitudes. However, this leakage/penetration of magnetospheric electric field is a numerical rather than a well-simulated physical effect since the model was not coupled with an inner magnetospheric model such as in the study by *Maruyama et al.* [2005]. This weak penetration electric field, however, did produce a simultaneous increase in TEC seen by the ground GPS receivers across several latitudes at 1630 UT [*Goncharenko et al.*, 2007]. The penetration electric field in our simulation is thus delayed about 10 min compared with the observations, which can be partly attributed to the fact that the TIEGCM outputs were saved in a 10-min cadence although the model itself was running in a 2-min time step.

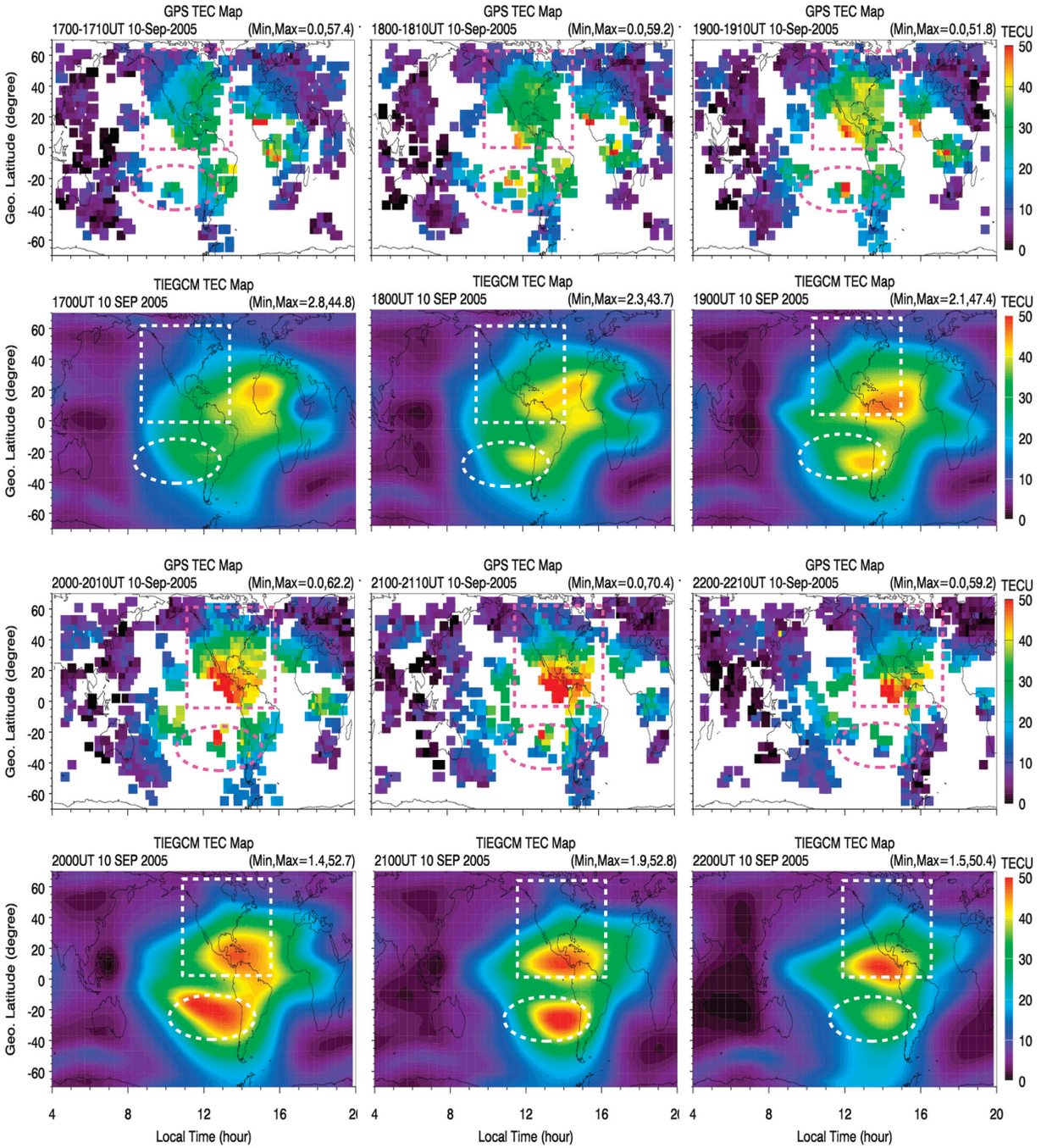

Plate 3. Comparison of measured GPS TEC and simulated TEC distributions.

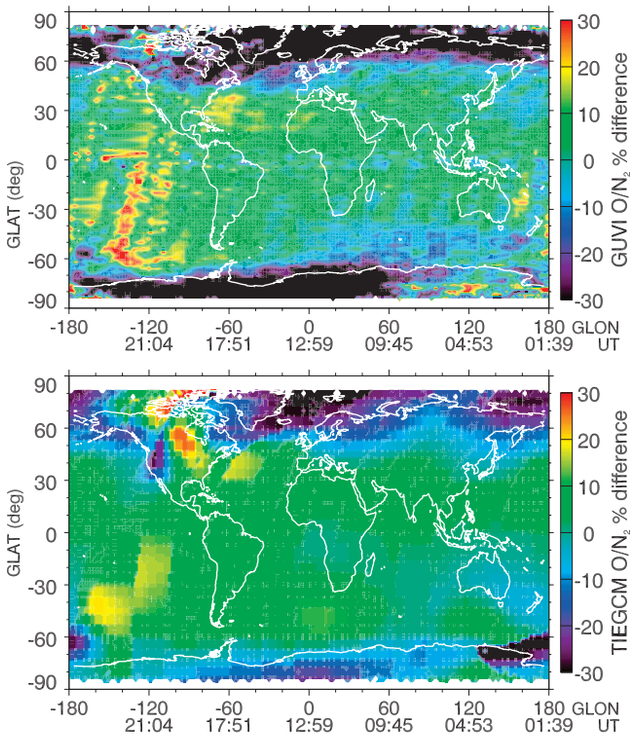

Plate 4. Comparison of the O/N_2 percent difference from the (top) GUVI measurements and (bottom) TIEGCM simulations.

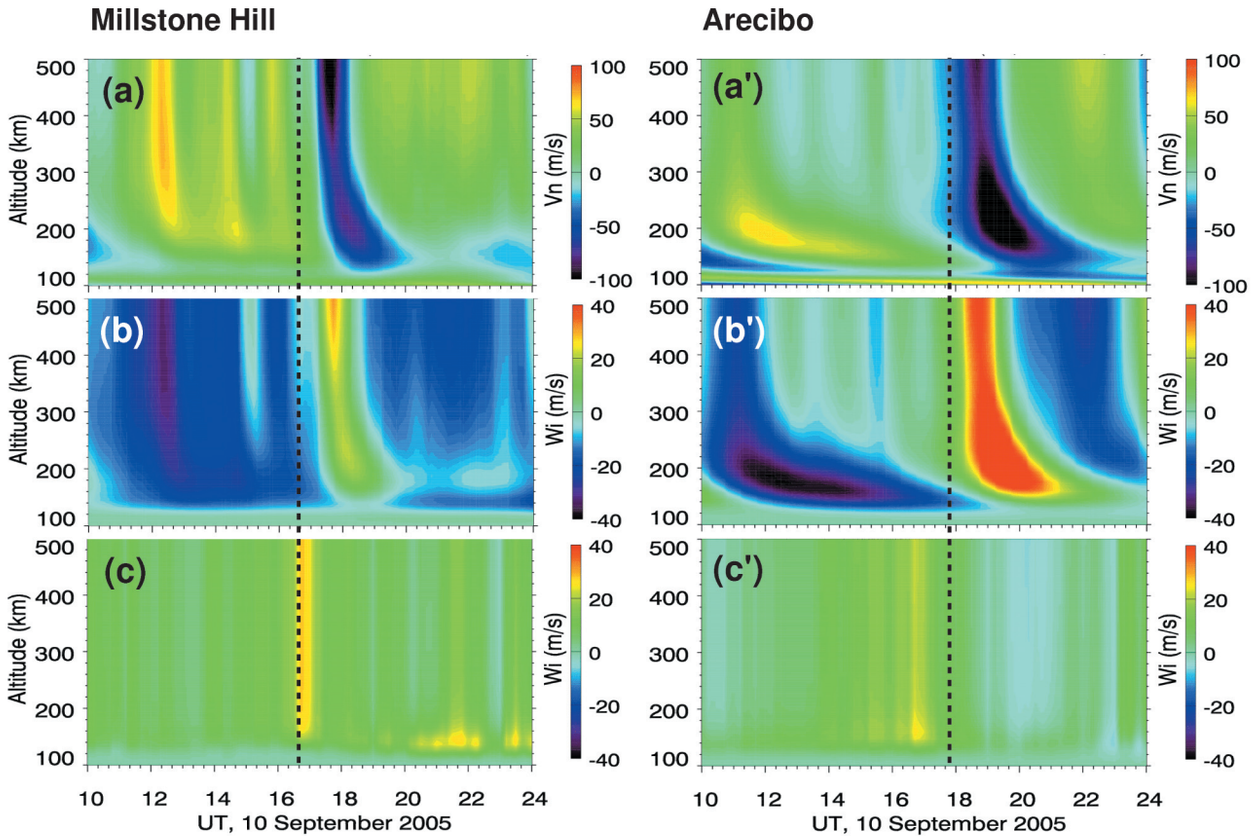

Plate 5. (a) and (a′) Simulated UT–altitude profiles of meridional wind, (b) and (b′) vertical ion drift due to neutral wind, and (c) and (c′) vertical ion drift due to electric field (bottom row). The vertical dashed lines mark the onset of the uplift of the electron density peak height over (left) Millstone Hill and (right) Arecibo. Positive value corresponds to northward meridional wind or upward ion drift.

As shown by *Lu et al.* [in press, Figure 3], there is a clear signature of traveling atmospheric disturbance in meridional wind, which propagates at a phase speed of ~700 m/s. The equatorward wind surge pushes ions upward in the northern hemisphere and downward in the southern hemisphere, with the demarcation near the local magnetic equator. However, there was very little change in zonal ion drift during the storm. They attributed the ineffectiveness for neutral winds to generate a disturbance dynamo field to the fact that the relatively large daytime *E* region conductivity may effectively short out the *F* region dynamo-driven currents, a mechanism proposed by *Rishbeth* [1997].

4. CONCLUSION

The comprehensive storm-time observations by the Millstone Hill and Arecibo radars provided an excellent opportunity to put the TIEGCM to a test. Although it was a moderate storm with a minimum *Dst* value of −70 nT and a maximum *AE* value of 2500 nT, the ionosphere exhibited some very interesting characteristics, such as the Λ-shaped profile of the *F* region electron density. Through the detailed data–model comparison, we have shown that the coupled AMIE–TIEGCM is able to reproduce many observed storm features of the ionosphere, including the Λ structure in the *F* region electron density profile. The quantitative error assessment indicates that our simulation results have an error of 1%–4% for h_mF_2, electron and ion temperatures at both radar locations during the 3-day period of 8–10 September 2005. The estimated error for N_mF_2 is about 9% at Millstone Hill and 19% at Arecibo. However, the simulated vertical ion drifts are less accurate, with the normalized RMS errors at 72% at Millstone Hill and 52% at Arecibo. The model is unable to capture the large temporal fluctuations shown in the radar observations, but it does reproduce reasonably well the overall large-scale variations during the 3-day period, including the storm-time-enhanced upward ion drift.

The TIEGCM simulations reveal that the primary cause of this dayside positive storm phase is the storm-enhanced meridional neutral wind. The enhanced joule heating in the high-latitude auroral zone produces a strongly equatorward/southward meridional wind surge that pushes plasma upward at midlatitudes. The subsequent northward wind associated with the rarefaction waves then pushes plasma downward, causing the *F* region peak height to drop. The neutral wind surges propagate in the form of gravity waves at a speed of ~700 m/s, consistent with the time delay observed between the two radars. The detailed component analysis of the simulated ion drift shows no significant dynamo electric field produced by the wind surges in this case study. Our simulations also confirm that for this particular storm event, both composition changes and the penetration magnetospheric electric fields have played a very minor role in producing the observed positive storm phase. Our study presented here is fully consistent with the previous findings by *Roble et al*. [1978], and it reiterates the importance of neutral wind effects on ionospheric disturbances.

Acknowledgments. We are grateful to many colleagues who provided various satellite- and ground-based data that have used in AMIE for this study. The ACE data were obtained from the NASA CDAW website. The work at HAO was supported under NASA's Sun–Earth Connection Guest Investigators and Living With a Star programs. Work at the Haystack Observatory was supported in part by the NASA grant NAG5-13602 and by NSF grant 0455831. NCAR is sponsored by the NSF. Millstone Hill radar observations and analysis are supported by an NSF cooperative agreement with MIT. The Arecibo Observatory is operated by Cornell University with support from a cooperative agreement with the NSF.

REFERENCES

Aponte, N., M. J. Nicolls, S. A. González, M. P. Sulzer, M. C. Kelley, E. Robles, and C. A. Tepley (2005), Instantaneous electric field measurements and derived neutral winds at Arecibo, *Geophys. Res. Lett.*, *32*, L12107, doi:10.1029/2005GL022609.

Blanc, M., and A. D. Richmond (1980), The ionospheric disturbance dynamo, *J. Geophys. Res.*, *85*, 1669–1686.

Buonsanto, M. J. (1999), Ionospheric storms—A review, *Space Sci. Rev.*, *88*, 563–601.

Burns, A. G., T. L. Killeen, G. R. Carignan, and R. G. Roble (1995), Large enhancements in the O/N_2 ratio in the evening sector of the winter hemisphere during geomagnetic storms, *J. Geophys. Res.*, *100*, 14,661–14,671.

Chamberlin, P. C., T. N. Woods, and F. G. Eparvier (2007), Flare Irradiance Spectral Model (FISM): Daily component algorithms and results, *Space Weather*, *5*, S07005, doi:10.1029/2007SW000316.

Field, P. R., H. Rishbeth, R. J. Moffett, D. W. Idenden, T. J. Fuller-Rowell, G. H. Millward, and A. D. Aylward (1998), Modeling composition changes in F-layer storm, *J. Atmos. Sol. Terr. Phys.*, *60*, 523–543.

Goncharenko, L. P., J. C. Foster, A. J. Coster, C. Huang, N. Aponte, and L. J. Paxton (2007), Observations of a positive storm phase on September 10, 2005, *J. Atmos. Sol. Terr. Phys.*, *69*, 1253–1272.

Hagan, M. E., and J. M. Forbes (2002), Migrating and nonmigrating diurnal tides in the middle and upper atmosphere excited by tropospheric latent heat release, *J. Geophys. Res.*, *107*(D24), 4754, doi:10.1029/2001JD001236.

Huang, C.-S., J. C. Foster, L. P. Goncharenko, P. J. Erickson, W. Rideout, and A. J. Coster (2005a), A strong positive phase of ionospheric storms observed by the Millstone Hill incoherent scatter radar and global GPS network, *J. Geophys. Res.*, *110*, A06303, doi:10.1029/2004JA010865.

Huang, C.-S., J. C. Foster, and M. C. Kelley (2005b), Long-duration penetration of the interplanetary electric field to the low-latitude ionosphere during the main phase of magnetic storms, *J. Geophys. Res.*, *110*, A11309, doi:10.1029/2005JA011202.

Lu, G., et al. (1996), High-latitude ionospheric electrodynamics as determined by the assimilative mapping of ionospheric electrodynamics procedure for the conjunctive SUNDIAL/ATLAS 1/GEM period of March 28–29, 1992, *J. Geophys. Res.*, *101*, 26,697–26,718.

Lu, G., L. P. Goncharenko, A. D. Richmond, R. G. Roble, and N. Aponte (2008), A dayside ionospheric positive storm phase driven by neutral winds, *J. Geophys. Res.*, *113*, A08304, doi:10.1029/2007JA01289.

Mannucci, A. J., B. T. Tsurutani, B. A. Iijima, A. Komjathy, A. Saito, W. D. Gonzales, F. L. Guarnieri, J. U. Kozyra, and R. Skoug (2005), Dayside global ionospheric response to the major interplanetary events of October 29–30, 2003 "Halloween Storms", *Geophys. Res. Lett.*, *32*, L12S02, doi:10.1029/2004GL021467.

Maruyama, N., A. D. Richmond, T. J. Fuller-Rowell, M. V. Codrescu, S. Sazykin, F. R. Toffoletto, R. W. Spiro, and G. H. Millward (2005), Interaction between direct penetration and disturbance dynamo electric fields in the storm-time equatorial ionosphere, *Geophys. Res. Lett.*, *32*, L17105, doi:10.1029/2005GL023763.

Mendillo, M. (2006), Storms in the ionosphere: Patterns and processes for total electron content, *Rev. Geophys.*, *44*, RG4001, doi:10.1029/2005RG000193.

Pawlowski, D. J., A. J. Ridley, I. Kim, and D. S. Bernstein (2008), Global model comparison with Millstone Hill during September 2005, *J. Geophys. Res.*, *113*, A01312, doi:10.1029/2007JA012390.

Prölss, G. W. (1993), On explaining the local time variation of ionospheric storm effects, *Ann. Geophys*. 1–9.

Prölss, G. W. (1995), Ionospheric F-region storms, in *Handbook of Atmospheric Electrodynamics*, edited by H. Volland, pp. 195–235, CRC Press, Boca Raton, Fla.

Richmond, A. D., and Y. Kamide (1988), Mapping electrodynamic features of the high-latitude ionosphere from localized observations: Technique, *J. Geophys. Res.*, *93*, 5741–5759.

Richmond, A. D., E. C. Ridley, and R. G. Roble (1992), A thermosphere/ionosphere general circulation model with coupled electrodynamics, *Geophys. Res. Lett.*, *19*, 601–604.

Rishbeth, H. (1989), F-region storms and thermospheric circulation, in *Electromagnetic Coupling in the Polar Clefts and Caps*, edited by P. E. Sandholt, and A. Egeland, pp. 393–406, Kluwer Acad., Norwell, Mass.

Rishbeth, H. (1997), The ionospheric E-layer and F-layer dynamo—A tutorial review, *J. Atmos. Sol. Terr. Phys.*, *99*, 1873–1880.

Roble, R. G., A. D. Richmond, W. L. Oliver, and R. M. Harper (1978), Ionospheric effects of the gravity wave launched by the September 18, 1974, sudden commencement, *J. Geophys. Res.*, *83*, 999–1009.

Schunk, R. W., and A. F. Nagy (2000), *Ionospheres—Physics, Plasma Physics, and Chemistry*, Cambridge Univ. Press, New York.

Tsurutani, B., et al. (2004), Global dayside ionospheric uplift and enhancement associated with interplanetary electric fields, *J. Geophys. Res.*, *109*, A08302, doi:10.1029/2003JA010342.

N. Aponte, Arecibo Observatory, HC03 Box 53995, Arecibo, P. R. 00612, USA.

A. J. Coster and L. P. Goncharenko, Haystack Observatory, Massachusetts Institute of Technology, Off Route 40, Westford, MA 01886-1299, USA.

G. Lu, A. D. Richmond, and R. G. Roble, High Altitude Observatory, National Center for Atmospheric Research, 1850 Table Mesa Drive, Boulder, CO 80305, USA. (ganglu@ucar.edu)

L. J. Paxton, Applied Physics Laboratory, Johns Hopkins University, 11100 Johns Hopkins Road, Laurel, MD 20723-6099, USA.